X-ray high-resolution vascular network imaging

Franck Plouraboué, Peter Cloetens, F Lauwers

X-ray high-resolution vascular network imaging

F. PLOURABOUÉ*, P. CLOETENS†, C. FONTA‡,¶, A. STEYER§,
F. LAUWERS¶ & J.-P. MARC-VERGNES¶
*I.M.F.T., UMR 5502, Allées du Pr. C Soula, 31400 Toulouse, France
†ESRF, BP 220, F-38043 Grenoble Cedex, France
‡CERCO UMR 5549, 133 route de Narbonne, 31062 Toulouse, France
§Université de Paris I, 75005 France
¶IFR96, I.S.C.T., U455 Service de Neurologie CHU Purpan, 31059 Toulouse Cedex 2, France

Key words. Brain, contrast agent, microtomography, microvascular, sample preparation, synchrotron radiation, X-ray.

Summary

This paper presents the first application of high-resolution X-ray synchrotron tomography to the imaging of large microvascular networks in biological tissue samples. This technique offers the opportunity of analysing the full three-dimensional vascular network from the micrometre to the millimetre scale. This paper presents the specific sample preparation method and the X-ray imaging procedure. Either barium or iron was injected as contrast agent in the vascular network. The impact of the composition and concentration of the injected solution on the X-ray synchrotron tomography images has been studied. Two imaging modes, attenuation and phase contrast, are compared. Synchrotron high-resolution computed tomography offers new prospects in the three-dimensional imaging of *in situ* biological vascular networks.

Introduction

Micro-vascular structural organization is an important physiological issue (Popel *et al.*, 1998) for which quantitative structural analysis is a key step. Indeed, there is growing interest in high-resolution imaging of vascular structures in different pathological issues, as recently reviewed (Weissleder & Mahmood, 2001). Promising microscopy techniques, such as two-photon microscopy, give the opportunity of screening localized *in vivo* physiological signals. Although very promising in many respects regarding functional *in vivo* signals, multiphoton laser microscopy is nevertheless still limited to about 200 µm depth (Brown *et al.*, 2001) and a restricted field of view. Moreover, the actual spatial resolution of *in vivo* measurements can be spoiled as a result of physiological fluctuations of the fluorescent markers. Other classical methods, such as scanning electron microscopy (Belisle & Sainte-marie, 1990; Reina-de la Torre *et al.*, 1998; Minnich *et al.*, 1999) or optical confocal microscopy (Cassot *et al.*, 1999), have been used for a systematic *in situ* study of vessel morphometry at the micrometre scale. Accurate as these methods may be, they are restricted to the investigation of tissue volume within a depth of a few hundreds of micrometres because the illuminating radiation has a finite penetration ability. Hence imaging larger volumes of tissue in any microscope requires sectioning them to a manageable thickness for the type of microscopy being used. Such sectioning can obviously damage the biological material and is followed by a non-obvious reconstruction step (Hanstede *et al.*, 1983). Hence, depending on the biological motivation, it is of interest to develop an alternative sample preparation method associated with a different imaging technique. New X-ray computed tomography (CT) tools permit a resolution better than 0·1 mm and open new perspectives for numerous structural studies (Elliot *et al.*, 1994; Momose *et al.*, 1996; Sasov & Van Dyck, 1997). The latest synchrotron X-ray sources permitting micrometre spatial resolution are the state-of-the-art tomography techniques and have already been used for imaging human trabecular bone structure (Peyrin *et al.*, 2000). In the context of vascular imaging, *in vivo* synchrotron tomography has allowed the measurement of contrast agent concentration and local blood flow on the whole brain of rats with the unprecedented spatial resolution of 350 µm (Elleaume *et al.*, 2002). This resolution still remains inadequate compared with the few micrometre scale of small vessels. Because 50% of the vessel diameters in the cerebral cortex lie between 3 and 10 µm, micrometre resolution is necessary to obtain important information regarding the vascular network at the scale of the small capillaries where the exchanges with the surrounding tissue take place. Although X-ray microtomography appears as a promising imaging

Correspondence to: Dr Franck Plouraboué. Fax: +33 05 61 28 58 99; e-mail: plourab@imft.fr

technique for microvascular structures, the sample nevertheless requires specific preparation. As recently discussed by Loo *et al.* (2001) there is still much to be done in the domain of biological tissue sample preparation in the X-ray domain compared with visible light techniques. Depending on the biological application, a specific preparation method is required. When visualizing bone (Kenney *et al.*, 1985; Peyrin *et al.*, 2000) or calcified tendons, one does not need to add any contrast agent because calcium is a sufficiently absorbing element for X-ray analysis. Nevertheless, X-ray absorption imaging of vascular structures requires specific contrast agents in order to enhance selectively the contrast between the capillaries and the surrounding tissue. For example, in the context of microfocus X-ray angiography, Dawson *et al.* (1999) have injected a bolus of iodinized molecules inside the pulmonary arterial tree. This type of injection allows us to visualize a specific region of interest (ROI) inside the whole network. The question of sample preparation is even more stringent in the context of high-resolution X-ray tomography.

The present paper describes, in its first part, a specific sample preparation method dedicated to analyse brain microvascularization using X-ray microtomography. The acquisition procedure of microtomography, both in absorption and in phase contrast mode, is introduced. The images obtained are finally discussed from a quantitative and qualitative point of view.

Methods

Sample preparation

Vascular networks are generally composed of very heterogeneous vessel sizes, from arterial to capillary level. Because the smallest capillary diameters are typically 3–4 μm in rat brains (and 5–6 μm in human brains), micrometre resolution is needed in order to image the smallest vessels of microvascular structures. When using micrometric resolution, the total accessible volume within a given three-dimensional (3D) image is obviously limited. The next section describes how a volume of just a few cubic millimetres can be accessible with our method. The attenuation signal expected from normal biological vascular tissue is nevertheless not sufficient to obtain satisfactorily contrasted images. One needs a specific sample preparation in order to improve the image contrast drastically. As usual in CT-scan angiography, a contrast agent can be injected inside the vascular network. Nevertheless, the contrast agent concentration needed for such small tissue volumes is much larger than those of CT-scan angiography. Moreover, the microvascular relative volume is generally quite small. In either human or rat brain, it represents only 3–5% of the total tissue volume. Hence, the effective vascular contribution to X-ray absorption or phase contrast represents a cumulated thickness of a few tens of micrometres only, along the few millimetres of the total X-ray path inside the tissue. Hence, sample preparation is a key step to obtain highly contrasted images suitable for automatic image segmentation.

The tissue sample preparation protocol consists of the following steps: surgery, injection, brain dissection and fixation, tissue sampling, sample dehydration and finally resin inclusion. It requires a few days to go from the living animal (adult rat) to the encapsulation of cylindrical tissue samples. The intracardiac injection itself follows different steps. An isotonic sodium chloride (0.9% NaCl) heparinized (0.1%) solution is first injected so as to obtain complete exsanguination. The rat body temperature is continuously maintained with an incubator lamp, with the injected fluid temperature kept at around 40 °C. A solution containing the contrast agent is then injected. Solutions of various compositions have been tested (see below).

The injection time is chosen such that, at the given flow-rate, the total brain vascular volume is perfused 20 times. After stopping the injection, the rat brain is dissected in a cooled dish (+4 °C) so that the gelatin in the injected solution thickens. The brain is then incubated in a 10% formalin bath for 24 h at 4 °C. After fixation, tissue samples are cut with a cylindrical surgical biopsy punch, which has an internal diameter of 3 mm. Each sample is then dehydrated into successive ethanol baths (from 30% to absolute alcohol), and finally incubated in propylene oxide. Samples are then impregnated into epoxy resin (EPON) using classical electron microscopy sample preparation. In order to facilitate tissue positioning during tomography measurements, samples are moulded into cylindrical resin casts. The external diameters of the cylindrical mould is 6 mm. The cast is bored with a cylindrical metallic drill of 3 mm diameter. The brain sample (original diameter of 3 mm has been reduced to approximately 2.5 mm due to tissue shrinkage occurring during dehydration) is inserted into a resin cylinder. After this preparation the total sample volume has been reduced by 20–30%.

Contrast agent solutions

The contrast agent consisted either of barium sulphate particles (Micropaque®, Guerbet) or of solute iron dextran (Anaemex®). Solid barium sulphate particles are micrometre sized and the molecular weight of iron dextran molecules is 5–10 kDa. These relatively large particles or molecular sizes prevent the contrast agent diffusing through the blood brain barrier inside the nervous tissue. Along with the contrast agent, a gelatin polymer is added into the injected solution. The role of gelatin is to prevent the contrast agent flowing outside the vessels once the injection is over. Different gelatin and contrast agent concentrations have been tested because there are contradictory constraints associated with these concentrations. Higher contrast agent concentration is better with regard to X-ray imaging. However, from the point of view of sample preparation, technical constraints limit the contrast agent concentration. The fluid pressure during injection must not be much higher than the physiological pressure and therefore the pump

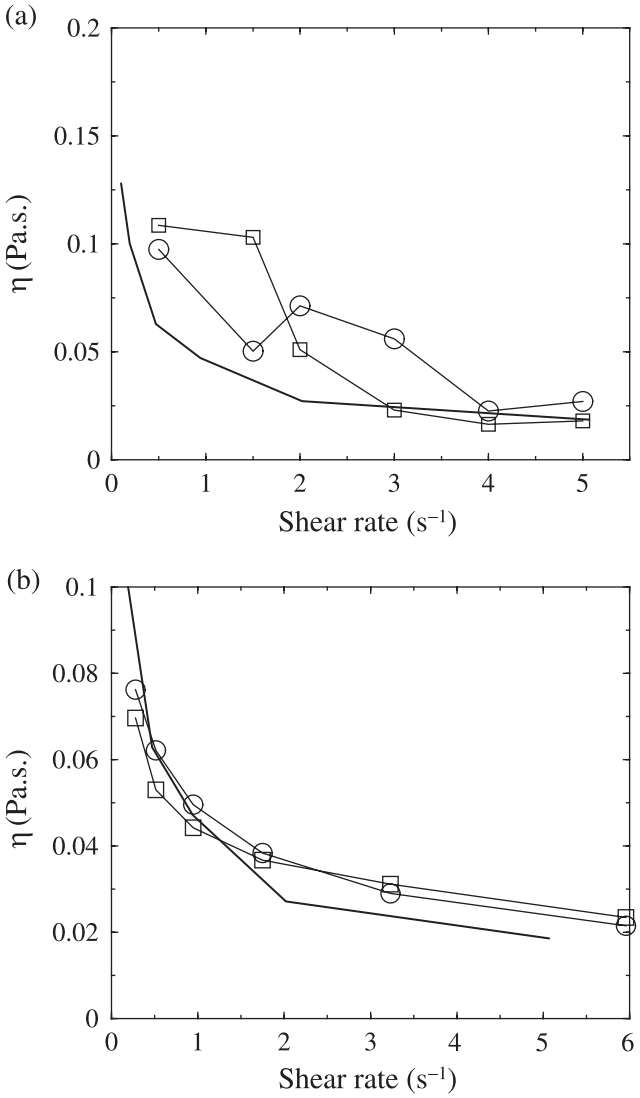

Fig. 1. (a) Viscosity of an iron dextran solution at 40 °C expressed as a function of the shear rate. The continuous curve is reference data for blood with 45% haematocrit extracted from Merrill (1969), circles and squares are associated, respectively, with iron dextran concentrations of 50 and 100 mg mL^{-1} with 2% gelatin. (b) As in (a) for micropaque barium sulphate viscosity with barium concentrations of 300 mg mL^{-1} (circles) and 600 mg mL^{-1} (squares) with 3% gelatin.

flow rate has to be adapted to the rheology of the injected solution. Like blood, the injected solution is a non-Newtonian fluid whose viscosity varies with shear rate. The viscosity decreases as shear rate increases. In order to quantify the impact of the solution composition on its rheology, we have measured the viscosity for different contrast agent and gelatin concentrations. We thus defined the concentration ranges of the different components suitable for the injection. The results are shown in Fig. 1(a,b) where the viscosity variation as a function of shear rate is compared with reference data for blood associated with a 45% haematocrit. In the range of investigated shear rates, both the iron dextran and barium solutions have quantitative rheological properties close to that of blood. This is an important condition for pressure not to exceed physiological values, and for injecting at a reasonable flow rate in an attempt to mimic physiological pressure drop.

A supplementary constraint comes from the fact that, at ambient temperature, the polymerization of gelatin is only observed for concentrations above 1 mg mL^{-1}. Hence, increasing contrast agent concentration while decreasing gelatin concentration for rheological considerations can only be done over a limited range. We have chosen iron dextran concentrations of 50–100 mg mL^{-1} and barium sulphate concentrations of 300–600 mg mL^{-1} with a gelatin concentration of 3–5%.

X-ray tomography

Third-generation synchrotron X-ray sources provide partially coherent, homogeneous and very bright photon beams. These beams are particularly interesting to investigate with high-spatial-resolution poorly contrasted objects. This section presents the basic principle of X-ray tomography, together with specific technical aspects related to our measurements. In general, the transmission of a wave through the sample is described by the complex transmission function $T(x,y)$ equal to the ratio of the exit wave and the incident wave:

$$T(x,y) = A(x,y)e^{i\varphi(x,y)}. \quad (1)$$

The amplitude $A(x,y)$ and the phase $\varphi(x,y)$ are related to the projection of the optical refractive index $n(x,y,z)$ of the sample, which depends on the sample composition and the incident wavelength λ. Synchrotron X-ray sources deliver a large X-ray energy spectrum. A wavelength adapted to the specimen under investigation is selected with a monochromator. At the experimental station ID19 of the European Synchrotron Radiation Facility used for the experiments (Cloetens *et al.*, 2002), the monochromator is either a double perfect silicon crystal monochromator (used at $E = 20$ keV) or a multilayer monochromator (used at photon energies E = 12 and 15 keV). We have investigated different imaging modes: attenuation and phase contrast. Attenuation contrast is related to the amplitude of the transmitted wave. Decomposing the complex refractive index n into its real and imaginary parts, it is usual to introduce two optical quantities δ and μ such that

$$n = 1 - \delta + i\frac{\lambda}{4\pi}\mu, \quad (2)$$

where the refractive index decrement δ is responsible for the phase modulation of the wave, and the linear attenuation coefficient μ affects the amplitude of the wave. The transmitted intensity $I_0(x,y)$ recorded immediately behind the sample (distance $D = 0$) is then related to the integral of the linear attenuation coefficient μ along the X-ray path inside the sample and to the incident uniform intensity I_{inc} by the relation:

$$I_0(x,y) = I_{inc}A(x,y)^2 = I_{inc}\exp[-\int \mu(x,y,z)dz]. \quad (3)$$

The quantity $\int \mu(x,y,z)dz$ is usually called the raysum and is measured in tomography for a large number of angular positions of the sample between 0 and 180°. In order to obtain an adequate dynamical range for the raysum, the transmitted intensity has to be recorded with a comparable dynamic range. A high-resolution X-ray detector system using a high-quality Peltier-cooled CCD (ESRF FreLoN camera) with 14-bit dynamic range and 2048×2048 pixels is used for that purpose. The X-ray signal is converted into visible light by a YAG:Ce converter screen. The spatial extent of the CCD pixels is 14 μm. Nevertheless, the spatial resolution can be much smaller by using a microscope objective coupling the converter screen to the CCD. The optics have been chosen such that the effective pixel size is 1.4 μm and the field of view 2.8 mm. The resin sample exterior diameter is 6 mm, and the biological cylindrical tissue diameter is close to 2.5 mm. The biological specimen itself is therefore always contained within the field of view and the part of the sample exceeding the field of view contains only homogenous resin. The local value of the linear attenuation coefficient μ inside the sample is related to the local atomic composition and density. The epoxy-resin X-ray attenuation is very close to water, and hence close to the average absorption of brain tissue. The linear attenuation coefficient of the injected solution trapped inside vascular vessels is mainly due to the absorption by the contrast agent and by water. It is interesting to compute this physical parameter so as to compare its value with that measured with X-rays and to choose the most adapted X-ray energy. The linear attenuation coefficient depends on the scattering cross-section σ of the absorbing atoms and their number per unit volume (Henke *et al.*, 1993). It can be expressed as a sum of the contribution of the different components of a mixture:

$$\begin{aligned}\mu_{sol} &= c_{ca} \cdot \left(\frac{\mu}{\rho}\right)_{ca} + \left(\rho_{sol} - c_{ca}\right)\left(\frac{\mu}{\rho}\right)_{w} \\ &= c_{ca} \cdot \left(\frac{\mu}{\rho}\right)_{ca} + \left(1 - \frac{c_{ca}}{\rho_{ca}}\right)\rho_{w}\left(\frac{\mu}{\rho}\right)_{w}\end{aligned} \quad (4)$$

where (μ/ρ) is the mass attenuation coefficient and the indexes sol, ca and w refer, respectively, to the solution, the contrast agent and the water. The second equality in Eq. (4) assumes that the different components of the solution are immiscible. The ratio of the contrast agent concentration and its density c_{ca}/ρ_{ca} is a small linear correction due to the volumic steric contribution of the contrast agent. The mass attenuation coefficient of a pure element with atomic weight A can be expressed as $\sigma \cdot N_A/A$ where N_A is Avogadro's number. From the tabulated values of the scattering cross-section, one obtains the variation of the linear attenuation coefficient with the radiation energy as represented in Fig. 2(a) for two concentrations of barium solutions: 300 and 600 mg mL^{-1}. One can compute the local contrast from the relative difference $(\mu_{sol} - \mu_w)/\mu_w$ between the linear attenuation coefficient of the injected solution and water with respect to the one of water, which will give an indication of the contrast quality of the reconstructed images. Figure 2(b) shows that both concentrations give good local contrast in the energy range of interest. More precisely, at the chosen energy of 20 keV, the local contrast between the barium solution and water is, respectively, equal to 12 and 22.2 for barium concentrations of 300 and 600 mg mL^{-1}. Another criterion for choosing the beam energy is related to the total transmission through the sample. It can be computed from knowledge of the vascular relative volume. The absorption inside the sample is due to the cumulative contribution of the epoxy-resin around and inside the biological sample and the injected solution inside the vascular network. The CCD detectors are optimally used when typically 80% of the incident intensity is absorbed, but they provide sufficient signal when being used at lower absorbed intensity. Figure 2(c) shows that the energy range between 15 and 20 keV provides absorption between 43 and 20% with the chosen sample diameter of 6 mm and with a vascular density of 3%, for both barium concentrations. This theoretical absorption calculation matches within 10% with the experimental measurements at $E = 20$ keV.

Phase contrast measurements are also possible with synchrotron radiation X-ray beams because they are partially coherent. As shown in Eq. (2) the real part of the refractive index is modified in the material by a small amount δ (~10^{-6}). This refractive index decrement is, far from absorption edges, proportional to the electron density and inversely proportional to the square of the photon energy. It is an alternative, and in general much more sensitive, source of contrast compared with the attenuation. The resulting contribution on the transmitted complex amplitude defined in Eq. (1) is the phase integrated along the X-ray path with respect to the same path in vacuum:

$$\varphi(x,y) = -\frac{2\pi}{\lambda}\int \delta(x,y,z)dz. \quad (5)$$

This phase modulation produces contrast due to Fresnel diffraction if the measurement, instead of being performed at the closest distance to the sample, is made at a finite distance D with respect to the sample. Assuming a relatively small distance, such that the radius of the first Fresnel zone $\sqrt{(\lambda D)}$ is small compared with the object features and the spatial resolution, the intensity $I_D(x,y)$ recorded at distance D is approximately

$$I_D(x,y) = I_0(x,y)\left[1 - \frac{\lambda D}{2\pi}\Delta_{xy}\varphi(x,y)\right] \quad (6)$$

with Δ_{xy} the 2D Laplacian (Cloetens *et al.*, 1997). The absorption image $I_0(x,y)$ recorded for a large number of angular positions allows us to determine the distribution of the linear attenuation coefficient μ through tomographic reconstruction. It can be shown (Cloetens *et al.*, 1997) that the same

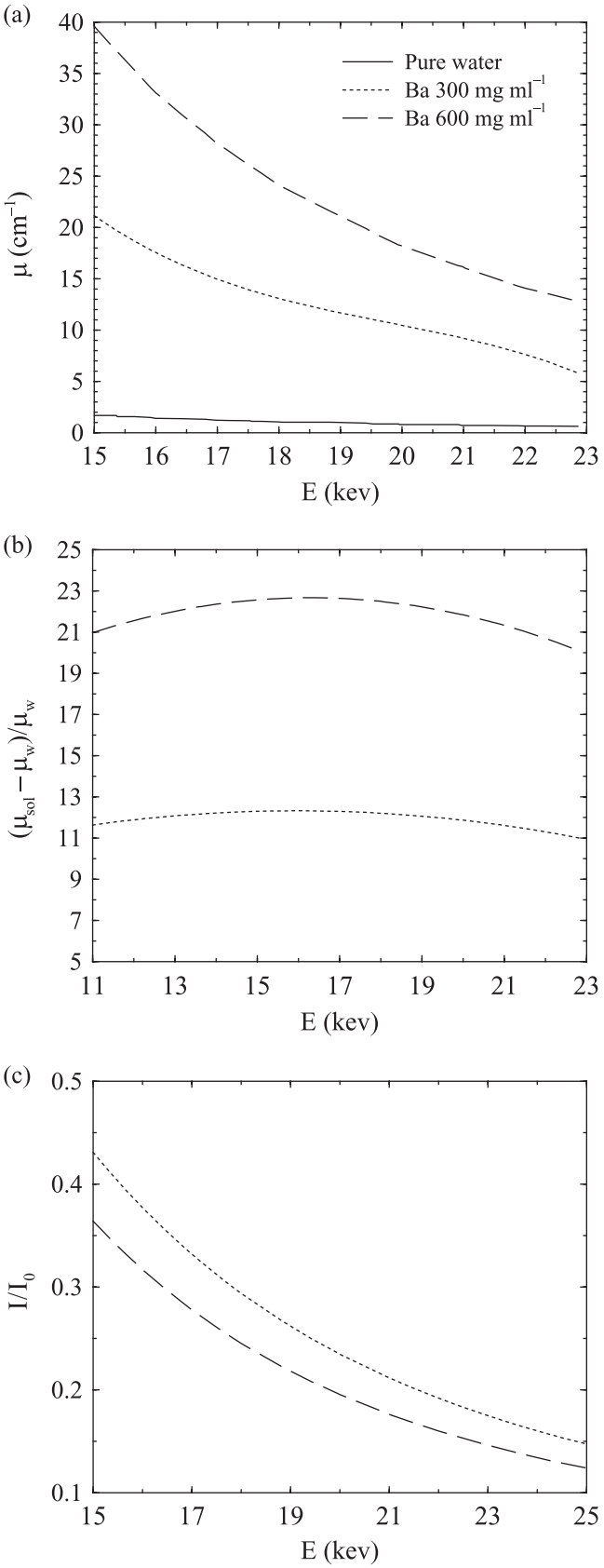

reconstruction algorithm applied to the images $I_D(x,y)$ results in the sum of two contributions: the usual attenuation coefficient μ and a second term equal to $-D \cdot \Delta_{xyz}\delta(x,y,z)$. The phase contrast contribution will therefore be strong in the tomographic reconstructions near regions where the density changes suddenly. A more quantitative approach consists in retrieving the phase $\varphi(x,y)$ from the defocused images $I_D(x,y)$ and using the result as input for the tomographic reconstruction. This combined approach, called holotomography, can be applied on biological tissues without contrast agent. However, it requires recording tomographic scans at different distances (typically four) and the resulting reconstruction would show all density changes, not selectively those related to the vascular network. For each tomographic scan 1200 projection images with the sample were recorded together with reference images without the sample. The tomographic reconstruction was performed using the usual filtered back-projection algorithm. Because the resin mould exceeds the field of view of the detector, the linear attenuation coefficient is reconstructed up to a constant equal to the coefficient of the resin, and will be denoted $\Delta\mu = \mu_{sol} - \mu_w$. The reconstructions have been performed on regions of interest tightly enclosed to the biological tissue and contain typically 1700^3 voxels.

Results and discussion

This section compares the results of computed tomography for different measurement modes (absorption and phase contrast) and for two different contrast agents (iron and barium solutions). We first present a quantitative analysis of the 3D images obtained and then discuss their quality and relevance.

The graphs shown in Fig. 3 have been obtained from the 3D attenuation maps of barium-injected samples for an X-ray energy of 20 keV and a sample–detector distance $D = 13$ mm. These histograms show two well-separated peaks. The first peak is associated with the epoxy, whereas the second corresponds to the contrast agent absorption in microvascular vessels. For each histogram, the second peak has a relative linear attenuation coefficient mode equal to $\Delta\mu = \mu_{sol} - \mu_w = 21.5 \pm 0.19$ cm^{-1}. The corresponding theoretical value represented in Fig. 2(a) given by Eq. (4) is $\Delta\mu = 17.4$ cm^{-1} at $E = 20$ keV. The agreement is reasonable, the relative error being 19%, between this rough theoretical estimate and the measurements. The observed variability on the second peak localization between samples extracted from the same injected rat brain is only of the order of a few per cent. This suggests that the observed

Fig. 2. (a) Linear attenuation coefficient as given by Eq. (4) and data from Henke *et al.* (1993). Continuous line is for pure water, whereas the dotted line and long dashed line are for barium sulphate solutions with barium concentrations, respectively, equal to 300 mg mL^{-1} and 600 mg mL^{-1}. (b) Local contrast of the linear attenuation coefficient with same convention as in (a). (c) Total absorbed intensity evaluated from Eq. (3) with same convention as in (a) and (b).

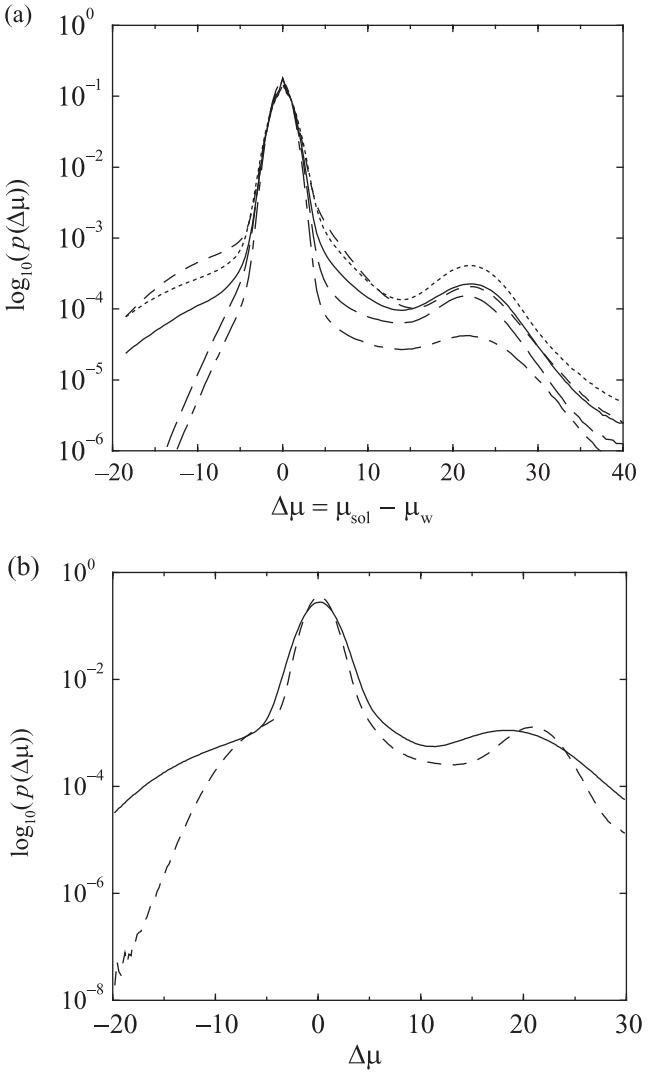

Fig. 3. (a) Probability distributions $p(\Delta\mu)$ of the relative linear attenuation coefficient $\Delta\mu = \mu_{sol} - \mu_w$ measured in absorption mode for five different cortical samples extracted from the same rat, for an injected barium concentration of 600 mg mL^{-1}. These histograms have been obtained by aggregating about 10^9 voxels. (b) Comparison of the histograms $p(\Delta\mu)$ of the relative linear attenuation coefficient $\Delta\mu = \mu_{sol} - \mu_w$ measured for a single barium-injected sample, in absorption (dotted line) and phase (continuous line) contrast mode.

difference between the injected barium concentration and the measured difference could be attributed to concentration effects, related to the *post mortem* dehydration process. It is interesting to compare the reconstructed values obtained for nearly pure absorption measurements and measurements containing significant phase contrast.

Figure 3(b) displays this comparison obtained on the same sample, with a distance of 13 mm for the absorption mode and of 25 mm for the phase contrast mode. The first peak associated with the epoxy background is essentially identical between the two measurements. There is nevertheless a much larger number of voxels with linear attenuation coefficient lower than the epoxy background in the phase contrast mode. The second peak associated with the barium contrast agent is obviously smoother for the phase contrast measure. Not only is the position of the second peak slightly shifted, but its overall width is significantly increased when the image contains a mixture of absorption and phase contrast at a distance of 25 mm. The shift to the left of the second peak should be attributed to its broadening. Indeed, observations result from a superposition of (at least) two independent contributions to the histogram: the first inside the vessel architecture, and the other in the epoxy background. Hence, this shift does not result from a physical difference related to an 'effective' relative linear attenuation coefficient but is rather the result of a statistical effect. By contrast, the broadening itself does result from a physical effect associated with intermediate fringes having pixels between white and black at density discontinuities located in the vicinity of vessel edges. This broadening could be first considered as producing lower image contrast. Images show just the opposite: Fig. 4(a,b) display a tomographic slice of the same barium-injected sample, imaged, respectively, in absorption and phase contrast mode. The grey level in the image scales linearly with the linear attenuation coefficient, high-absorption regions such as injected vessels appearing white. The inset images in Fig. 4(a,b) illustrate that the local contrast of the phase mode is higher than in the absorption mode. Some vessels almost disappear in Fig. 4(a) (indicated by arrows) whereas they are clearly visible in Fig. 4(b). This local increase in image contrast is due to the phase signal coming from the vessel edge. The difference between both measurements is depicted in Fig. 4(c); the inverse grey levels show that the difference is at a maximum at the vessel boundaries. This is because phase measurements at small distances are most sensitive to density discontinuities at the vessel boundaries, which are associated with density variations between endothelial cells and epoxy. A careful inspection of Fig. 4(c) also shows that small vessels can be better detected by phase measurement than absorption alone, using for example region growth methods (Vignoles, 2001) rather than simple thresholding.

Let us now turn to volume renderings of the resulting 3D images obtained using Amira® software (TGS). Figure 5(a–c) display maximum intensity projections of barium-injected samples. The vessel density observed on these images illustrates the quality of the preparation, and the apparent high vessel density of the rather loose vascular network results from the projection over a 1-mm thickness. It can be seen that the infiltration depth of the contrast agent spreads over the entire sample depth, so that a dense microvascular network is visible. Some preliminary image analysis indicates that the observed vascular density varies from 5 to 10% of the total volume. This result is consistent with previous observations (e.g. Reina-de la Torre *et al.*, 1998) and indicates that the infiltration has been almost complete. A more careful inspection of

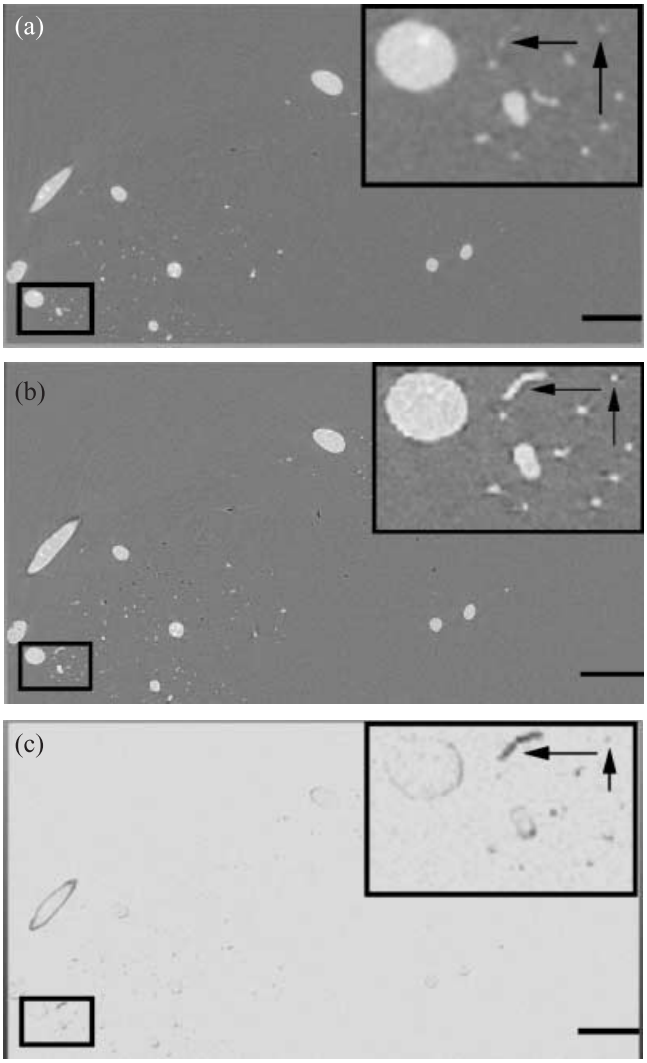

Fig. 4. Tomographic slice of a barium-injected sample with (a) a sample-to-detector distance $D = 13$ mm, (b) $D = 25$ mm, (c) the difference between (a) and (b). The X-ray energy was 20 keV. Scale bar = 100 μm. The upper right inset is a 4× magnification of the lower rectangular area.

the obtained images also displays an extremely small number of dead-end vessels that could be associated with partially infiltrated small vessels. These renderings are also interesting to visualize the quality of the local vessel contrast obtained with the highest barium concentration (600 mg mL^{-1}). The images show columnar structures that spread through the grey matter depth from the pial surface, as described in Duvernoy (1995). It can be observed that the orientation of these vascular columns, reminiscent of neuronal cortical columns, is more or less orthogonal to the cortical surface. The in-depth extent of those arterial vessels appears heterogeneous, varying by more than a factor of two in Fig. 5(c). Those intracortical vessels were classically divided into 3–6 groups according to their degree of cortical penetration (Duvernoy *et al.*, 1981).

Other interesting views are presented in Fig. 5(d,e) in order to give a better indication of the 3D vascular network in the cerebral cortex. Those renderings are, to our knowledge, the first visualization of the vascular structure of the cortex grey matter over its entire thickness, at the micrometre scale. Their quantitative morphometric analysis should be interesting from various points of views: to obtain the first quantitative measurement of the spatial extent of the vascular cortical columns, as well as the heterogeneity of their associated vascular density in relation to the distance to the pial surface. This point has already been mentioned with regard to the human brain cortex by Duvernoy *et al.* (1981) and Reina-de la Torre *et al.* (1998). The organization of the vascular network at this columnar level could now be analysed from the obtained images over the entire grey matter over 2–3 mm depth. This is an important achievement in the context of microvascular investigations that no other microscopy technique can offer. It is moreover interesting to compare the quality of the reconstructed tomography images obtained from preparations injected with a different contrast agent. Figure 6(a,b) display renderings of a rat cortex injected with a 100 mg mL^{-1} iron dextran and 3% gelatin solution. The images obtained display drastically less dense vascular projections than those obtained with barium (cf. Fig. 5). Furthermore, the contrast of an injected vessel compared to the image background is significantly poorer than that obtained with barium. The histograms of iron-dextran-injected samples do not show two well-separated peaks, excluding automatic image segmentation. These observations are consistent with the theoretical calculations, from which the contrast expected for barium injections is about seven times larger than that expected from iron dextran injections as a result of the higher concentration and the larger scattering cross-section. The smallest vessels cannot be detected within the epoxy background, because they may have been poorly injected with iron dextran contrast agent. Infiltration of the contrast agent is then far more homogeneous in the case of barium-injected solutions than for iron dextran.

Conclusions

Our results clearly show that synchrotron X-ray tomography opens new perspectives in the analysis of the microvascular architecture of biological tissues. A specific sample preparation method dedicated to this purpose has been described. A voxel resolution of 1.4 μm was achieved over the millimetre range, to obtain 3D tomography reconstructions with a size of several cubic millimetres. Injections with barium sulphate as contrast agent at a concentration of 600 mg mL^{-1} prove to be the most successful in terms of both sample preparation and image quality in absorption mode. Phase-sensitive imaging enhances the contrast of the smallest capillaries and of poorly injected vessels. This technique has been successfully applied to the vascular cortical network. It has permitted us

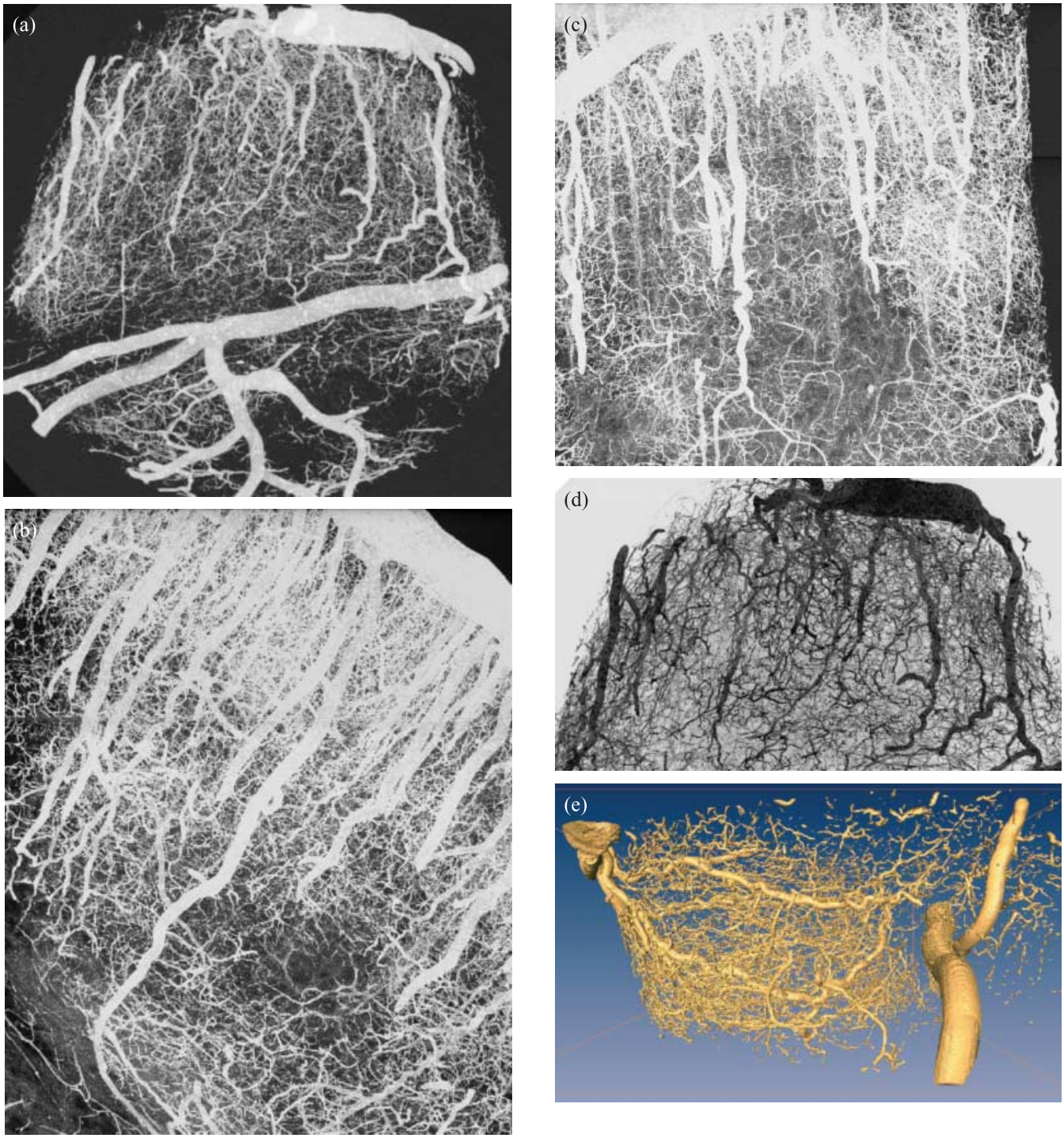

Fig. 5. Volume renderings of a sample injected with barium (600 mg mL^{-1}), obtained at 20 keV in absorption mode with a voxel size equal to 1.4 µm. The images correspond to different samples extracted from different cortical regions of the same rat. Maximum intensity projections have been performed for volumes with a size equal to Δx = 1.5 mm, Δy = 1.5 mm, Δz = 1 mm: (a) Projection in the x–y plane of a sample extracted from the fronto-central region; (b) projection in the y–z plane of a sample extracted from the frontal cortex; (c) x–z projection of the same sample as in (b); (d) close-up view on the x–y plane projection of (a), using an in-depth coding in grey levels; (e) 3D iso-surface view of sample (a) in the z–y plane.

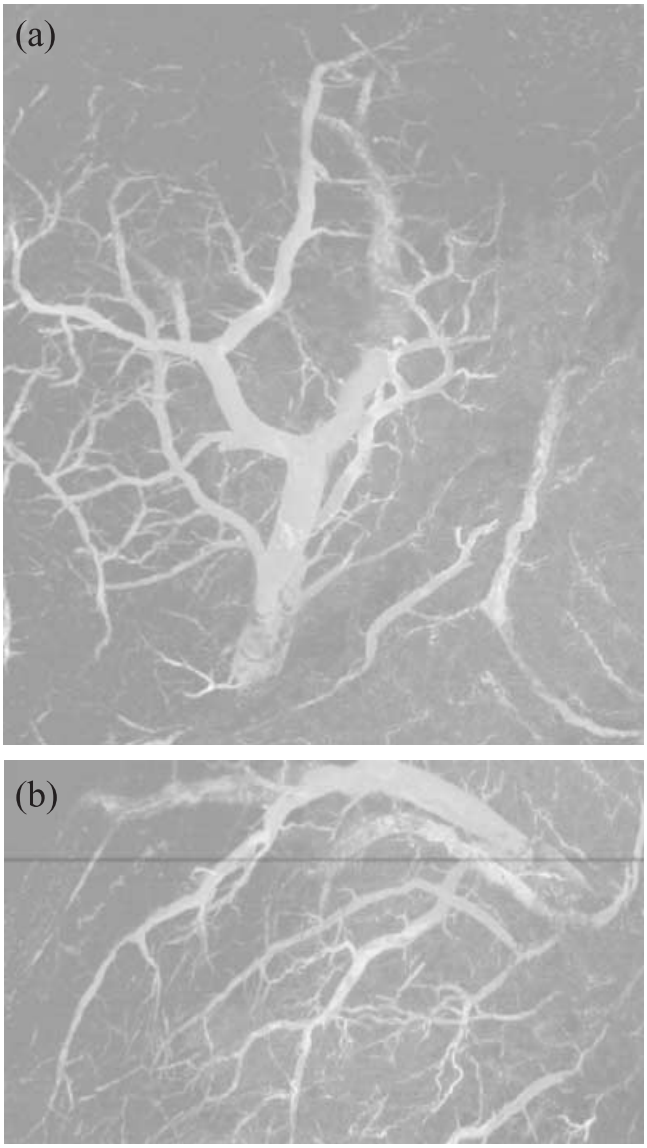

Fig. 6. Volume renderings of a sample injected with iron dextran (100 mg mL^{-1}) obtained in absorption mode with a voxel size equal to 1.4 µm. The images correspond to the same sample extracted from the frontal rat cortex. Maximum intensity projections have been performed for volumes with a size equal to Δx = 1.5 mm, Δy = 1.5 mm, Δz = 1 mm: (a) projection in the x–y plane; (b) projection in the y–z plane.

to image for the first time in three dimensions the vascular structure of the grey matter of a rat cerebral cortex over its entire depth. A similar sample preparation method and imaging procedure can be applied to human brain tissue. Quantitative analysis of the 3D images will provide important morphometric information of interest in different contexts in which the microvascularization plays a key role, such as physiological and pathological angiogenesis and brain functional imaging (fMRI) whose basic principles rely on cortical microvascularization.

Acknowledgements

We thank Professor Terissol and his team for providing useful physical data for the X-ray absorption computations. Thanks to Didier Asselot from TGS, Elodie Boller, François Estève, Géraldine Leduc, Françoise Peyrin, Steffen Prohaska, Laurent Risser and Xavier Thibault for their help and support. We acknowledge Luc Renaud, Grégory Dhoye, Cédric Trupin, Sébastien Cazin, Pierre Ferré and François Esteban for technical support.

References

Belisle, C. & Sainte-marie, G. (1990) Blood vascular network of the rat lymph node: tridimensional studies by light and scanning electron microscopy. *Am. J. Anat*. **189**, 111–126.

Brown, E.B., Campbell, R.B., Tsuzuki, Y., Xu, L., Carmeliet, P., Fukumura, D. & Jain, R.K. (2001) In vivo measurements of gene expression, angiogenesis and physiological function in tumors using multiphoton laser scanning microscopy. *Nature Med.* **7**, 864–868.

Cassot, F., Paulin-Laurens, P., Plouraboué, F., Duvernoy, H. & Marc-Vergnes, J.P. (1999) Morphometric study of a human microvascular network. *J. Cereb. Flow Metab*. **708**, 21–37.

Cloetens, P., Ludwig, W., Boller, E., Peyrin, F., Schlenker, M. & Baruchel, J. (2002) 3D imaging using coherent synchrotron radiation. *Image Anal. Stereol*. **21** (Suppl. 1), S75–S85.

Cloetens, P., Pateyron-Salomé, M., Buffière, J.Y., Peix, G., Baruchel, J., Peyrin, F. & Schlenker, M. (1997) Observation of fatigue failure in composites by phase sensitive radiography and tomography. *J. Appl. Physiol*. **81**, 5878–5886.

Dawson, C.A., Krenz, G.S., Karau, K.L., Haworth, S.T., Hanger, C.C. & Linehan, J.H. (1999) Structure–function relationships in the pulmonary arterial tree. *J. Appl. Physiol*. **86**, 569–583.

Duvernoy, H.M. (1995) *The Human Brain Stem and Cerebellum*. Springer-Verlag, New York.

Duvernoy, H.M., Delon, S. & Vannson, J.L. (1981) Cortical blood vessels in the human brain. *Brain Res. Bull*. **7**, 519–579.

Elleaume, H., Charvet, A.M., Corde, S., Estève, F. & Le Bas, J.F. (2002) Performance of computed tomography for contrast agent concentration measurements with monochromatic X-ray beams: comparison of k-edge versus temporal subtraction. *Phys. Med. Biol*. **47**, 3369–3385.

Elliot, J.C., Anderson, P. & Davis, G.R. (1994) Computed tomography, II. The practical use of a single source and detector. *J. Microsc*. **126**, 11–19.

Hanstede, J.G. & Gerrits, P.O. (1983) The effect of embedding in water-soluble plastics on the final dimensions of liver sections. *J. Microsc*. **131**, 79–86.

Henke, B.L., Gullikson, E.M. & Davis, S.C. (1993) *Atomic Data and Nuclear Data Tables*, 54, 2, 181–342.

Kenney, J.M., Jacobsen, C., Kirz, J., Rarback, H., Cinotti, E., Thomlinson, W., Rosser, R. & Schidlovsky, G. (1985) Absorption microanalysis with a scanning soft X-ray microscope: mapping the distribution of calcium in bone. *J. Microsc*. **138**, 321–328.

Loo, B.W., Sauerwald, I.M., Hitchcock, A.P. & Rothman, S.S. (2001) A new sample preparation method for biological soft X-ray microscopy: nitrogen-based contrast and radiation tolerance properties of glycol methacrylate-embedded and sectioned tissue. *J. Microsc*. **204**, 69–86.

Merrill, F.W. (1969) Rheology of blood. *Physiol. Rev*. **49**, 863–888.

Minnich, B., Leeb, H., Bernroider, N. & Lametschwandtner, A. (1999) Three-dimensional morphometry in scanning electron microscopy: a technique for accurate dimensional and angular measurements of microsctructuresusing stereopaired digitized images and digital image analysis. *J. Microsc.* **195**, 23–33.

Momose, A., Takeda, T., Itai, Y. & Hirano, K. (1996) Phase contrast X-ray computed tomography for observing biological soft tissues. *Nature Med.* **2**, 473–475.

Peyrin, F., Salome, M., Nuzzo, S., Cloetens, P., Laval-Jeantet, A.M. & Baruchel, J. (2000) Perspectives in three-dimensional analysis of bone samples using synchrotron radiation microtomography. *Cell. Mol. Biol.* **46**, 1089–1102.

Popel, A.S., Pries, A.R. & Slaaf, D.W. (1998) Developments in the microcirculation physiome project. *J. Neuro. Meth.* **111**, 911–913.

Reina-de la Torre, F., Rodriguez-Baeza, A. & Sahuquillo-Barris, J. (1998) Morphological characteristics and distribution pattern of the arterial vessels in human cerebral cortex: a scanning electron microscope study. *Anat Record*, **251**, 87–96.

Sasov, A. & Van Dyck, D. (1997) Desktop X-ray microscopy and microtomography. *J. Microsc.* **191**, 151–158.

Vignoles, G.L. (2001) Image segmentation for phase-contrast hard X-ray CMT of C/C composites. *Carbon*, **39**, 167–173.

Weissleder, R. & Mahmood, U. (2001) Molecular imaging. *Radiology*, **219**, 316–333.